









RESEARCH ARTICLE | JANUARY 02 2025

## Electrical properties of ScN thin films controlled by defect engineering using oxygen ion implantation

Charlotte Poterie ; Hugo Bouteiller ; Razvan Burcea ; Sylvain Dubois ; Per Eklund ; Arnaud Le Febvrier  ; Thierry Cabioch ; Jean-François Barbot  



*J. Appl. Phys.* 137, 015101 (2025)  
<https://doi.org/10.1063/5.0230961>



### Articles You May Be Interested In

Effect of induced defects on conduction mechanisms of noble-gas-implanted ScN thin films

*J. Appl. Phys.* (August 2023)

Defect engineering-induced Seebeck coefficient and carrier concentration decoupling in CuI by noble gas ion implantation

*Appl. Phys. Lett.* (November 2024)

Strategies to enhance the performance of thermoelectric materials: A review

*J. Renewable Sustainable Energy* (June 2023)



Journal of Applied Physics

Special Topics Open  
for Submissions

[Learn More](#)





# Electrical properties of ScN thin films controlled by defect engineering using oxygen ion implantation

Cite as: J. Appl. Phys. 137, 015101 (2025); doi: 10.1063/5.0230961

Submitted: 27 July 2024 · Accepted: 11 December 2024 ·

Published Online: 2 January 2025



Charlotte Poterie,<sup>1</sup>  Hugo Bouteiller,<sup>1,a)</sup>  Razvan Burcea,<sup>1,2</sup>  Sylvain Dubois,<sup>1</sup>  Per Eklund,<sup>3,4</sup>   
Arnaud Le Febvrier,<sup>3,4,b)</sup>  Thierry Cabioc'h,<sup>1</sup>  and Jean-François Barbot<sup>1,b)</sup> 

## AFFILIATIONS

<sup>1</sup>PPRIME Institute, CNRS, Université de Poitiers—ENSMA, UPR 3346, SP2MI, TSA 41123, 86073 Poitiers cedex 9, France

<sup>2</sup>SPMS, Centrale Supélec, Université Paris-Saclay, Gif-sur-Yvette, France

<sup>3</sup>Department of Physics, Chemistry and Biology (IFM), Linköping University, SE-581 83 Linköping, Sweden

<sup>4</sup>Inorganic Chemistry, Department of Chemistry—Ångström, Uppsala University, Box 538, SE-751 21 Uppsala, Sweden

<sup>a)</sup>Present address: Materials Science and Technology Division, Oak Ridge National Laboratory, Oak Ridge, Tennessee 37831, USA.

<sup>b)</sup>Authors to whom correspondence should be addressed: arnaud.le.febvrier@liu.se and jean.francois.barbot@univ-poitiers.fr

## ABSTRACT

Defects tend to modify significantly the properties of semiconductors, such as transport properties, by increasing the scattering of electrons and phonons, or optical properties, by modifying the band structure and the Fermi level. The high interest of ScN thin films for thermoelectric applications results from the incorporation of oxygen, which is well known to be the source for their degenerate n-type state and their significant power factor. Indeed, oxygen acts as a donor defect when substituted to nitrogen. In this study, oxygen ion implantation was performed at a high damage level as a way to modify electrical properties through defect engineering. Hence, we measured the changes in electrical properties induced by oxygen implantation at room temperature. Two types of defects have been identified as being responsible for the change in resistivity, carrier concentration, mobility, and Seebeck coefficient. At first, the point-like defects, recombining from 440 K and onward, introduce localized states near the Fermi level, inducing a change in the conduction mode from a metallic-like to a hopping mechanism. The relationship between Mott's temperature and defect concentration has been clearly demonstrated through *in situ* resistivity measurements in the 80–750 K temperature range. Furthermore, these measurements highlight that oxygen induced defects result not only from ballistic effects, but also from chemical effects that are involved. Second, the complex-like defects introduce deep acceptor levels into the bandgap and act as scattering centers that modify the Debye temperature as well as the electron–phonon interactions. These complexes, likely between scandium vacancies and oxygen atoms ( $V_{\text{Sc}}\text{-yO}$ ,  $y \leq 4$ ), are primarily responsible for the increase of the Seebeck coefficient and the reduced mobility. The concentration of such defects can qualitatively be assessed as their formation introduces an additional term, independent of temperature, in the variation of resistivity, mobility, and also the Seebeck coefficient. The recovery of the complex-like defects takes place at a minimum temperature of 750 K. Results show that the effectiveness of oxygen in creating defects exceeds that of noble gases in terms of concentration, demonstrating the promise of this approach to control the electrical properties of ScN.

© 2025 Author(s). All article content, except where otherwise noted, is licensed under a Creative Commons Attribution (CC BY) license (<https://creativecommons.org/licenses/by/4.0/>). <https://doi.org/10.1063/5.0230961>

## I. INTRODUCTION

Scandium nitride (ScN) is a degenerated semiconductor with an indirect bandgap of approximately 1 eV. It has received considerable attention in recent years as nitride semiconductors for optoelectronic applications and for its potential thermoelectric (TE)

applications.<sup>1</sup> The interest for TE applications is driven by its substantial power factor ( $\text{PF} = S^2/\rho$ , with  $S$  being the Seebeck coefficient and  $\rho$  the electrical resistivity),<sup>2,3</sup> comparable to conventional materials, such as  $\text{Bi}_2\text{Te}_3$ ,<sup>4</sup>  $\text{PbTe}$ ,<sup>5</sup> and  $\text{SiGe}$ .<sup>6</sup> However, the thermal conductivity of ScN, ranging from 11 to 20  $\text{Wm}^{-1}\text{K}^{-1}$  at room

temperature (RT), is excessively high for routine thermoelectric applications, prompting ongoing research into methods to reduce it, such as alloying<sup>7–9</sup> or ion implantation.<sup>10,11</sup> Scandium nitride (ScN) thin films exhibit *n*-type conductivity with high carrier concentration in the degenerate range of  $10^{20}$ – $10^{22}$  cm<sup>-3</sup>. The reason for such high doping arises from the substitution of nitrogen by oxygen ( $O_N$ ),<sup>3,12</sup> usually in the form of contamination during the deposition process.<sup>13</sup> The presence of oxygen in substitution does not drastically alter the electronic band structure, but moves the Fermi level into the conduction band.<sup>3,14</sup> Other defects with negative formation energies act as donors, such as nitrogen vacancies ( $V_N$ ) or fluorine and tantalum substituting for nitrogen ( $F_N$  and  $Ta_N$ ).<sup>15</sup> However, the concentration of these donor defects strongly depends on the deposition conditions and the purity of the target,<sup>16</sup> and consequently, their effect on the doping of the films is usually negligible compared with oxygen. The high *n*-type doping is also achieved as acceptor defects, such as scandium vacancies ( $V_{Sc}$ ), antisites, or oxygen interstitials ( $O_i$ ), have high positive formation energy<sup>15</sup> and, thus, are not favorable. More generally, a better understanding of the defects, whatever their type, is needed to control or monitor the transport properties of materials for thermoelectric applications.

By its nature, ion implantation ensures a non-equilibrium configuration in the implanted material. This is due to the ballistic nature of the process, in which impurity ions of various species are introduced into a host matrix, regardless of its metallurgical compatibility. Once an implanted ion becomes immobilized, the system can relax to a lower-energy configuration, closer to an equilibrium structure. This phenomenon also contributes to the formation of defects of various types and dimensionalities. Consequently, this process is commonly used in the microelectronics industry for doping and/or creating defects as in the Smart Cut™ process, for example.<sup>17</sup> More recently, ion implantation has proven its use for engineering thermoelectric materials by tuning their carrier concentration and improving the thermoelectric power factor.<sup>4,10,11,18–24</sup> It has been effectively utilized with various ions ( $Li^+$ ,  $Ar^+$ , and  $Mg^+$ ) to substantially decrease the thermal conductivity of ScN films highlighting the role of defects in phonon scattering.<sup>10,11,24</sup> The Seebeck coefficient is also increased, which is beneficial for TE applications; however, a high control of the defects created is needed in order to better control the resistivity increase that occurs after implantation.

In the present study, oxygen ions were implanted at a high damage level (dpa: displacement per atom), almost ten times higher than in previous investigations involving noble gas implantation (Ar and He).<sup>11,23</sup> Oxygen is assumed to be electrically active.<sup>15</sup> Hence, a homogeneous damage level (9 dpa) throughout the film thickness for a concentration between 1% and 2% of implanted oxygen was reached to ensure that chemical effects were not minimized or overlooked. The effects of both atom dopants and implantation-related defects have been investigated through electrical measurements.

## II. EXPERIMENTAL DETAILS

Degenerate *n*-type ScN thin films were implanted using oxygen ( $O^+$ ) ions. DC reactive magnetron sputtering in an ultra-high vacuum chamber was used to deposit epitaxial-like ScN films onto MgO substrates, with the orientation relationship: [111](111)

ScN || [111](111) MgO. More details on the deposition chamber can be found elsewhere.<sup>25</sup> A power of 120 W was applied on a 2-in. Sc target (Mateck/99.95%). The working pressure during depositions was kept at 2 mTorr for a 68% Ar/32%  $N_2$  sputtering gas-mixture. The films were deposited onto one side-polished  $10 \times 10$  mm<sup>2</sup> MgO(111) substrates, which were heated at 900 °C and under constant rotation. Prior to deposition, the substrates were cleaned using detergent steps (described elsewhere<sup>26</sup>), followed by a 10 min ultrasonic bath of acetone, then of ethanol, and finally blown dry with a  $N_2$ -gun. These deposition steps ensure good crystalline quality,<sup>27</sup> thus limiting oxidation at the surface and through the grain boundaries.<sup>28</sup>

The films were implanted with oxygen ions ( $O^+$ ) at room temperature (RT) and at 773 K (500 °C) using the EATON VN3206 implanter, under an approximate vacuum of  $1 \times 10^{-6}$  mbar. The beam current was kept below 12  $\mu A$  for the films implanted at RT to avoid any additional heating of the substrate, while for the films implanted at 773 K, the beam current was increased up to 30  $\mu A$ . The SRIM 2013 software was used under the full-damage cascade<sup>29</sup> to determine the depth profiles of the O ions implanted into ScN using its theoretical density of 4.27 g cm<sup>-3</sup>. To reach a homogeneous damage level throughout the film thickness, three acceleration energies were used. The doses for each energy were chosen to obtain a homogeneous total damage level of nine displacement per atom (9 dpa), i.e.,  $2 \times 10^{16}$ ,  $5.2 \times 10^{15}$ , and  $2.8 \times 10^{15}$  cm<sup>-2</sup>, respectively, for 120, 50, and 25 keV. The damage depth profiles for each energy and the corresponding concentration of oxygen reaching a cumulative value  $\sim 1.5$  at. % are presented in Fig. 1. A former experiment has shown with argon implantation that damage regimes larger than 1 dpa enable the tuning of electrical properties and conduction modes.<sup>23</sup> In addition, it showed that a saturation regime was reached after 3–4 dpa. Therefore, the choice for an implantation at 9 dpa is justified by the high doping rate of the sample.

Following its implantation at RT, the corresponding film was annealed using two devices depending on the annealing temperature. After implantation, the film was annealed *in situ* while measuring the resistivity, interrupting each measurement at 500, 600, and 750 K. For each temperature, the *in situ* annealing was carried out under no specific atmosphere and at a constant speed of 3 K min<sup>-1</sup>. For temperatures above 875 K, the annealing steps were performed in a dedicated furnace for 10 min at constant temperature under a vacuum of  $5 \times 10^{-6}$  Pa. These annealing steps are referred as “*ex situ*,” while the previous ones below 750 K are referred as “*in situ*.”

Macroscopic in-plane resistivity  $\rho(T)$ , charge carrier density  $n(T)$ , and mobility  $\mu(T)$  were measured using ECOPIA HMS-5500, which combines the van der Pauw method with the Hall effect. It uses two setups: a cryostat setup for temperatures from 80 to 350 K using liquid nitrogen and one for high temperature with temperature ranging from 300 to 750 K. The mobility is calculated using  $\rho(T)$  and  $n(T)$  following  $\mu(T) = \frac{1}{\rho(T)n(T)e}$ , with  $e$  being the elementary charge. A constant magnetic field of 0.580 T was applied for the Hall measurements. *In situ* annealing was performed using these two setups.

The Seebeck coefficient  $S(T)$  was measured with the Physical Properties Measurement System (PPMS, Quantum Design) using a

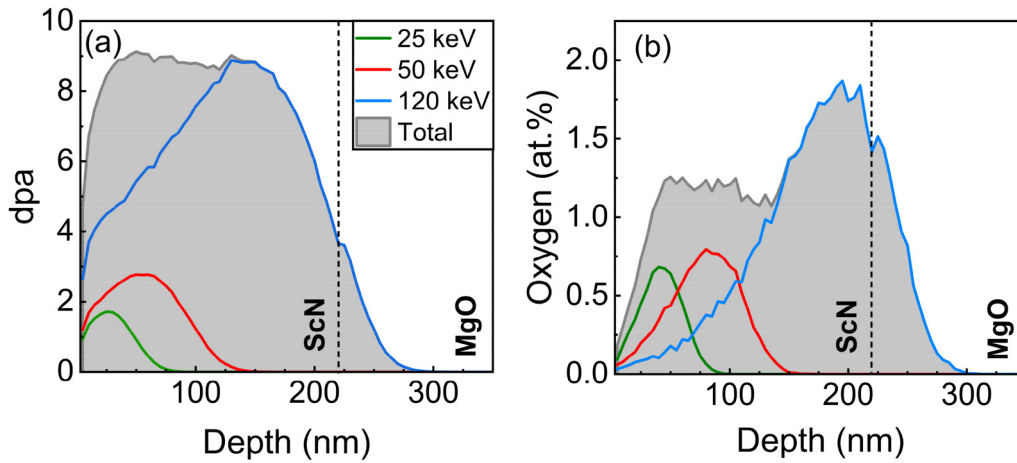


FIG. 1. (a) Displacement per atoms (dpa) and (b) concentration profiles as a function of depth calculated using the SRIM code for multi-energy O-9 dpa implantation.

linear four-probe configuration. In this configuration, the resistivity can also be measured at a very low temperature. Therefore, below 80 K, in-plane resistivity is measured with this system.

### III. RESULTS AND DISCUSSION

#### A. Overview on an implantation effect

Figure 2 shows the resistivity  $\rho(T)$  and the mobility  $\mu(T)$  of the ScN thin film in its initial state (labeled as Reference) and implanted with  $O^+$  at 9 dpa at RT (labeled as O-9 dpa) in the temperature range of 80–300 K. Below 110 K, the reference  $\rho(T)$  appears nearly constant while it increases linearly with increasing

temperature above ( $d\rho/dT > 0$ ). This metallic-like behavior is characteristic of highly degenerate semiconductors and is in good agreement with the large charge carrier density measured, i.e.,  $\bar{n}_e = 2.2 \pm 0.2 \times 10^{21} \text{ cm}^{-3}$ . This value of the carrier concentration is attributed to oxygen incorporated during the film deposition and is found to be constant with temperature leading to a decrease of  $\mu(T)$ . The Seebeck coefficient at RT, around  $-22 \mu\text{V K}^{-1}$ , is relatively low for the reference state that can be explained by the high carrier concentration/metallic-like behavior of the as-grown ScN. Its negative value confirms the  $n$ -type conductive behavior. TE materials are supposed to be optimized in a “moderately” degenerate state with a carrier concentration between  $10^{19}$  and  $10^{20} \text{ cm}^{-3}$ .<sup>30</sup>

21 January 2025 14:57:36

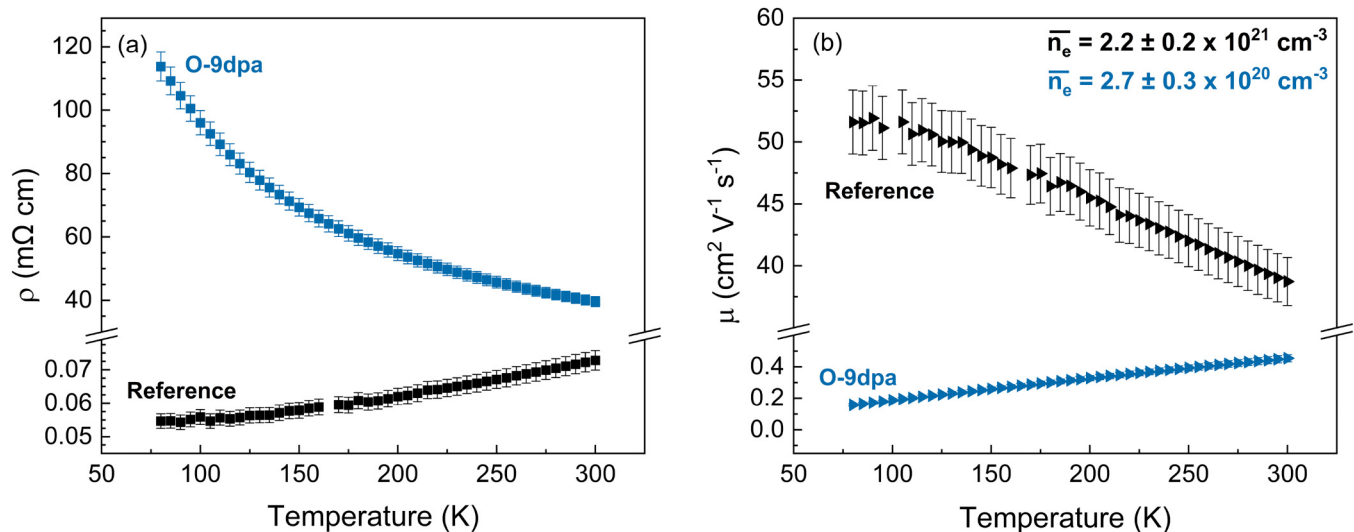


FIG. 2. Comparison of the electrical transport properties of the reference and implanted ScN samples (O-9 dpa) with (a) resistivity and (b) mobility in the temperature range of 80–300 K.

Once implanted with oxygen (O-9 dpa), a drastic change is observed in the electrical properties of the film. The resistivity has gained two to three orders of magnitude with the values at RT, at 39 mΩ cm. In addition, the temperature-dependent resistivity has changed ( $dp/dT < 0$ ), characteristic of semiconductor-like behavior. The carrier concentration remaining constant over the temperature domain is also reduced to  $\bar{n}_e = 2.7 \pm 0.2 \times 10^{20} \text{ cm}^{-3}$ , hence close to ten times lower. Moreover, after ion implantation, the Seebeck coefficient is enhanced from  $-22$  to  $84 \mu\text{V K}^{-1}$  at RT. Its linear behavior in temperature is analyzed in detail in Sec. III E.

These observations when implanting ions into the ScN thin films are comparable to those already reported with Ar and He implantations.<sup>11,23</sup> The change in the conduction mode from metallic (as-deposited state) to semiconducting behavior (implanted state) was ascribed to the creation of point-like defects that induce localized states close to the Fermi level. Furthermore, the decrease of the carrier concentration was explained by the creation of argon-vacancy complex implantation-defects, which, in turn, form deep acceptor levels in the bandgap. These defects were presumed to be the results of ballistic effects induced by the noble gas implantation process.<sup>11</sup> Interestingly, the changes or effects observed after O-implantation (O-9 dpa) are much pronounced than those reported with noble gases, where defect saturation was observed as early as 3–4 dpa.<sup>23</sup> It suggests that oxygen implantation leads to the formation of a higher concentration of defects as well as different types of defects. One challenge regarding the use of oxygen is the possibility of promoting the oxidation of films. The reference sample has limited oxidation due to its good crystallinity.<sup>27</sup> Furthermore, the measurements are reproducible through time and samples, which indicates that the effects of possible oxidation remain limited with respect to the electrical properties of the films. As a result, the effect of oxidation on the properties was discarded in favor of implantation-related defects.

## B. Conduction mechanism in the low temperature regime (4–300 K)

Temperature-dependent electrical resistivity of semiconductors is given by

$$\rho(T) = \rho_0 \exp \left[ \left( \frac{E_t}{k_B T} \right)^p \right], \quad (1)$$

where  $\rho_0$  is the resistivity coefficient,  $E_t$  the transition energy, and  $p$  a characteristic component ( $p > 0$ ) defining the mode of electrical conduction.<sup>31</sup> Electrical conduction can be achieved by band conduction, which is thermally activated or through hopping of the charge carriers between localized states. With decreasing temperature, hopping mechanisms can vary from Nearest Neighbor Hopping (NNH) to Variable Range Hopping (VRH). For NNH conduction, carriers hop to localized states in the impurity donor band, while for VRH conduction, hopping takes place between the localized states close to the Fermi level. VRH mechanisms can be of two types depending on the temperature: Mott-VRH introduced by Mott<sup>32</sup> and ES-VRH presented by Efros and Shklovskii for lower temperatures.<sup>33</sup> Mott-VRH, where the Coulomb interaction between electrons is neglected, considers a constant density of state (DOS) close to the Fermi level. In Table I, the exponent  $p$ , the

**TABLE I.** Characteristic energies, exponents, and temperatures of the different electrical conduction modes in semiconductors with  $L_C$  representing the localization length,  $N(E_F)$  the density of states (DOS),  $k_B$  the Boltzmann constant, and  $\epsilon$  the dielectric constant.<sup>31</sup>

Conduction mechanism	Characteristic energy $E_t$	Exponent $p$	Characteristic temperature $T_t$
Band conduction	$E_a$	1	...
NNH	$E_a^{NNH} < E_a$	1	...
Mott-VRH	$E_M = k_B T_M$	0.25	$T_M = \frac{18}{L_C^2 N(E_F) k_B}$
ES-VRH	$E_{ES} = k_B T_{ES}$	0.5	$T_{ES} = \frac{2.8 \epsilon^2}{\epsilon L_C k_B}$

characteristic energy  $E_t$  for different mechanisms, and the characteristic temperature for the VRH mechanisms are listed. In the case of ES-VRH happening at a very low temperature, the Coulomb interactions cannot be neglected anymore, as the system is not energetic enough to overcome those interactions between carriers, which leads to a Coulomb gap.

Further investigations of the semiconducting mechanisms taking place in the implanted film at the low temperature regime (4–300 K) are presented in Fig. 3. The change in the slope around 40 K, with a sharp rise in resistivity up to 4 K, Fig. 3(a), reveals a different conduction mechanism than at a higher temperature. Between 4 and 40 K,  $\ln(\rho)$  exhibits a linear dependence function of  $T^{-0.5}$  [Fig. 3(b)], while above 80 K,  $\ln(\rho)$  is linear with  $T^{-0.25}$  [Fig. 3(c)]. This highlights the change in the dominant electrical conduction mechanism, ES-VRH for  $T < 40$  K, and the Mott-VRH hopping mechanism for a higher temperature  $T > 80$  K, at least up to 300 K [see Fig. 3(a)]. Consequently, the dominant electrical conduction operating in Fig. 2(a) is Mott-VRH conduction. The characteristic Mott-VRH conduction temperature  $T_M = E_t/k_B$  calculated from the slope is estimated to be about  $T_M \sim 18\,800$  K. This value (O-9 dpa) is much higher than that reported for argon, which was found to remain unchanged at around 16 K beyond 3–4 dpa.<sup>23</sup>  $T_M$  gives qualitative information on the defect concentration as it is inversely proportional to the cube of the localization length (Table I) and, hence, shows that an extremely high density of point-like defects is generated during oxygen implantation.

Previous experiments with noble gases have shown that the point-like defects responsible for this change in the conduction mode could be related to clustering of self-interstitials ( $Sc_i$  and  $N_i$ ) caused by ballistic effects.<sup>23</sup> Indeed, the noble gas defects do not introduce shallow levels, which ensured that the electrical properties were not modified by any chemically induced defects. These ballistic induced defects are created for any implanted ion as it is dependent on nuclear processes. However, chemical effects are at play since oxygen is electrically active when forming substitutional ( $O_N$ ) or interstitial ( $O_i$ ) defects,<sup>15</sup> hence introducing shallow or deep levels, respectively. Calculations have shown that the DOS and the Fermi level were not modified in the same way depending on the generated defects. Indeed, Sc or N vacancies ( $V_{Sc}$  or  $V_N$ ) lead to more changes in the band structure and the DOS than  $O_N$  defects, especially by introducing states close to the Fermi level.<sup>14,34,35</sup> Similar observations were made on ScMn<sub>2</sub>-type phases where  $O_N$  did not lead to the creation of energy states close to the Fermi level

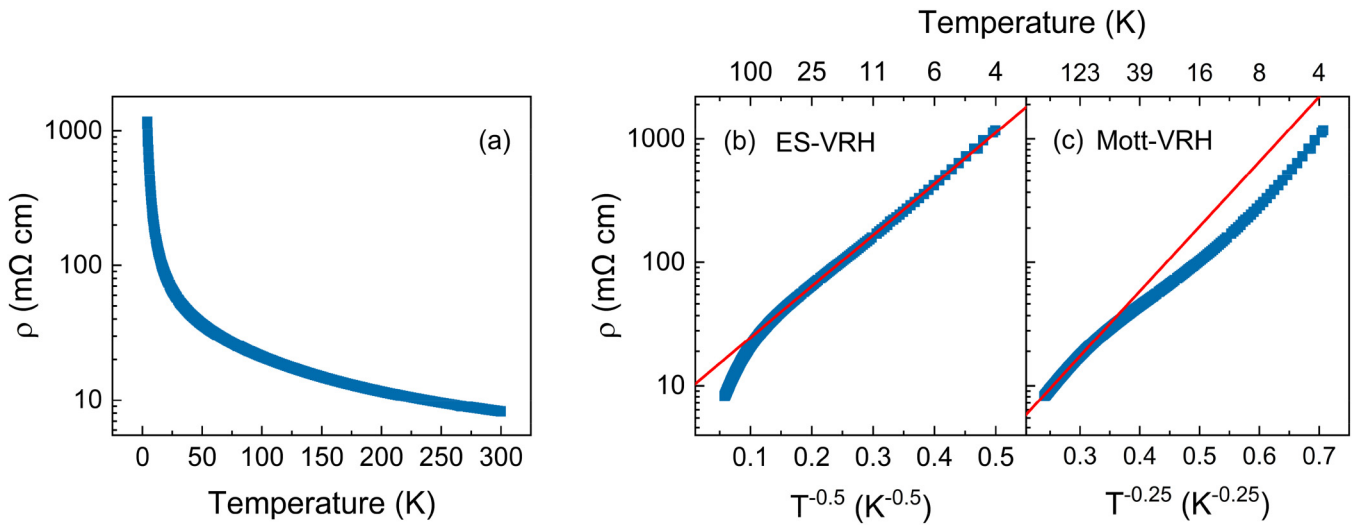


FIG. 3. (a) Resistivity of the implanted ScN on a log-scale vs  $T$  highlights the change in slope and, therefore, the change of the conduction mechanism in the temperature range of 4–300 K. The log-scale resistivity vs (b)  $T^{-0.5}$  and (c)  $T^{-0.25}$  is represented with their linear domains emphasized by straight lines (red).

unlike  $V_N$ .<sup>34</sup> Interstitial and vacancy defects have high formation energy, which decreases their formation probability at equilibrium.<sup>15</sup> The benefit in using implantation is that it creates non-equilibrium configurations, enabling the formation of these defects. Moreover, point defects, such as  $V_{Sc}$  and  $O_i$ , act as acceptor defects.<sup>15</sup> Thus, the high concentration of point-like defects after oxygen implantation is the result of defects created by ballistic effects as well as the oxygen defects induced by chemical effects.

### C. Recovery of point-like defects

The resistivity measurements of the *in situ* annealing steps are presented in Fig. 4. The implanted film (O-9 dpa) was first measured until 500 K (blue points). The film was then cooled down to 80 K and the measurement was run again from 80 to 600 K (red). The same process was followed for the next two measurements, performed from 80 to 750 K (green and then orange, respectively). For each step, the resistivity exhibits reversible semiconducting behavior ( $\leftrightarrow$ ) in a temperature range extending up to the previous measurement. Beyond the previous temperature at which the *in situ* annealing was stopped, a sharp increase in the slope is observed, after which the behavior is no longer reversible ( $\rightarrow$ ). This decrease of electrical resistivity and irreversibility clearly shows the activation of another mechanism similar to the one observed in  $Ar^+$  and  $Mg^+$  implanted ScN thin films and which was attributed to the recombination of point-like defects.<sup>23,24</sup> After annealing up to 750 K (orange), the reversible region extends all the way to 750 K and the metallic-like behavior of the reference samples is recovered above 300 K, which highlights that the point-like defects are close to fully recombined.

The Mott-VRH temperatures  $T_M$  were calculated and are listed in Table II. Upon successive annealing,  $T_M$  decreases, nearly reaching 0 K once the metallic behavior is recovered. With  $T_M$

being inversely proportional to the cube of the localization length  $L_c$ , these variations during *in situ* anneals (Table II) result from the decrease in the density of the localized states, directly linked to the generation of point-like defects, and their nearly complete

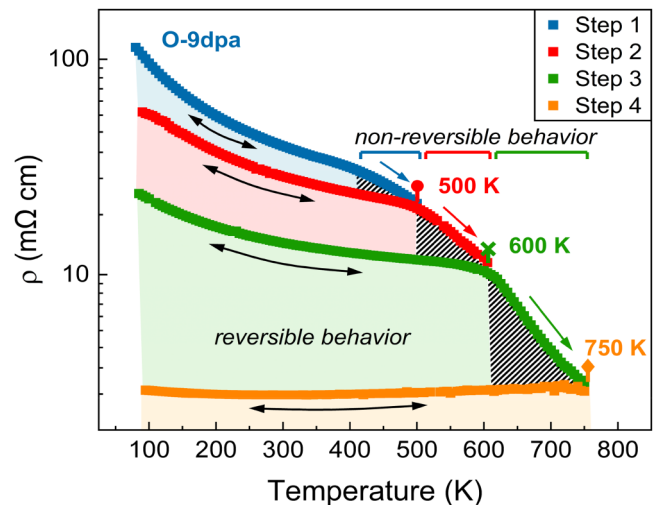


FIG. 4. Electrical resistivity vs temperature of the implanted ScN (O-9 dpa) undergoing several *in situ* annealing steps: (i) the film is cooled down to 80 K, and (ii) the measurement is run to the desired temperature. This process was repeated four times, to measure up to 500 K first, then 600 K, and, finally, two times up to 750 K. The reversible behavior of  $\rho(T)$  is shown by two-way black arrows along with the colored region, while the single-colored arrows along with the hatched regions illustrate the region where point-like defects are recombining.

21 January 2025 14:57:36

**TABLE II.** Variation of the Mott temperature ( $T_M$ ) as a function of temperature steps of the previous *in situ* measurement and, thus, in relation to the state of ScN.

State of the film	Implanted	500 K	600 K	750 K
$T_M$ (K) $\pm$ 5%	18 800	9200	1400	0.5

recombination at 750 K. The recombination of these defects not only leads to a change in the conduction mode but also in a partial release of the carriers, as the carrier concentration increases to  $\bar{n}_e = 5.5 \pm 0.5 \times 10^{20} \text{ cm}^{-3}$  after the annealing at 750 K. The recent reports with noble gases (Ar and He) have attributed the decrease in the carrier concentration only to the complex-like defects. Indeed, the reduced concentration observed after implantation remained constant after the recombination of all point-like defects. Meanwhile, in the present study, once the point defects induced by oxygen implantation are recombined, the carrier concentration has been increased, compared to the implanted state. The activation energy of recombination has been estimated through the *in situ* successive measurements using an Arrhenius model. It has been estimated to increase from  $E_{a, \text{implanted}} = 80 \pm 10 \text{ meV}$  to  $E_{a, 600 \text{ K}} = 345 \pm 10 \text{ meV}$  after the 600 K annealing. The activation energy found after implantation ( $E_{a, \text{implanted}}$ ) is similar to that reported for argon implantation,<sup>23</sup> which indicates that the defects recombining are of the same type, i.e., resulting from ballistic effects. At a higher temperature, larger activation energy indicates the recombination of other point-like defects. Their recombination leads to a release of the charge carriers. Hence, these defects correspond to the electrically active oxygen defects, i.e., resulting from chemical effects. Such results demonstrate that predominantly

acceptor point-like defects are created, such as interstitial oxygen ( $O_i$ ) and scandium vacancies ( $V_{\text{Sc}}$ ), which modify the density of states.<sup>14,15</sup>

#### D. Recovery of complex-like defects

*Ex situ* annealing steps were carried out at temperatures from 875 to 1375 K where only complex-like defects remained at a temperature above 875 K. As shown in Fig. 5, beyond 875 K, both resistivity and mobility gradually recover with increasing annealing temperature, in concomitance with the carrier release. This suggests that the implantation-related complex-like defects of acceptor-type recover (or undergo transformation) during annealing. However, even after annealing at 1375 K, the degenerated semiconductor properties are not fully restored, showing that there are still defects affecting the electrical properties, as previously reported for Ar-5dpa implanted ScN.<sup>11</sup> Even after high temperature annealing (1375 K), the mobility is still close to half that of the reference state, highlighting a scattering effect of these complex-like defects.

The metallic-like behavior of resistivity, Fig. 5, for  $T > T_0 = 110 \text{ K}$ , can be described by the following equation:

$$\rho(T) = \rho_R + \alpha(T - T_0) + \rho_{\text{CD}}, \quad (2)$$

with  $\alpha$  being the slope of the curve,  $\rho_R$  the residual resistivity, and  $\rho_{\text{CD}}$  the additional resistivity induced by the complex-like defects created during the implantation process. The residual  $\rho_R$  was estimated from the reference curve and kept constant for the implanted/annealed curves,  $\rho_R = 0.036 \text{ m}\Omega \text{ cm}$ . The contribution of introduced complexes could be estimated once all point defects were recombined,  $\rho_{\text{CD}, 750 \text{ K}} \sim 2.2 \text{ m}\Omega \text{ cm}$ . This value, larger than that observed for

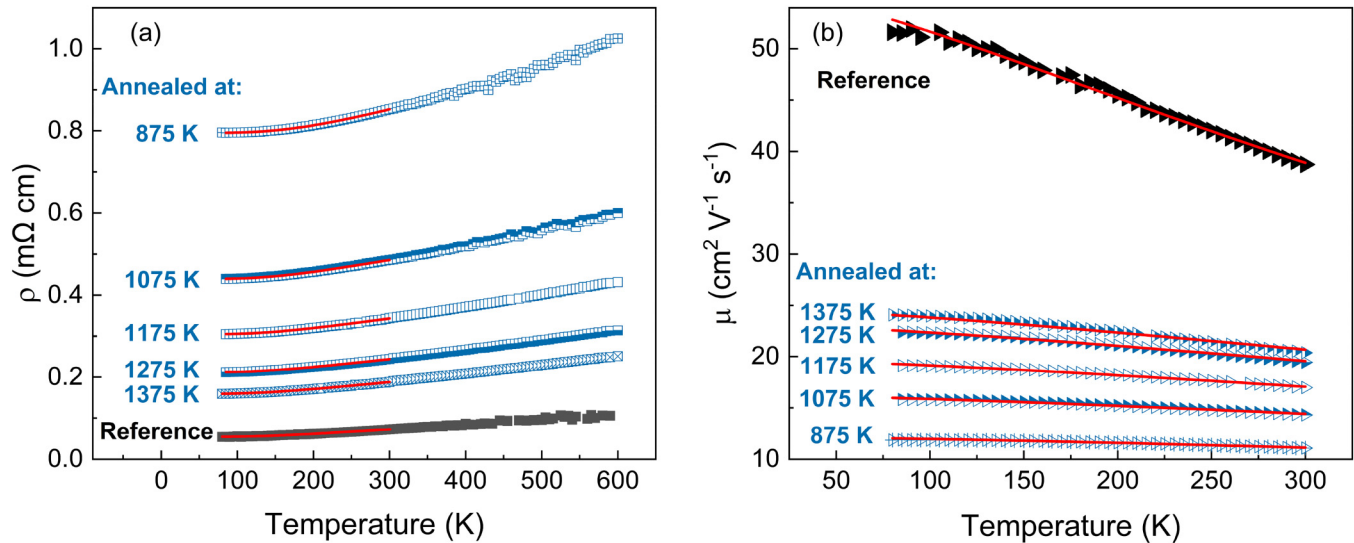


**FIG. 5.** (a) Resistivity and (b) mobility vs temperature of the implanted ScN (0-9 dpa) undergoing subsequent *ex situ* annealing (875–1375 K). Different models were used and are represented by the red lines: (a) Bloch–Grüneisen model [Eq. (3)] below 300 K to describe the electrical resistivity and (b) the Matthiessen model [Eq. (4)] to describe the mobility.

argon (Ar > 3 dpa), highlights the ability of oxygen to create defects of a stable nature, including vacancy-type defects as reported for noble gases. Moreover, recent first-principles calculations have shown that oxygen readily forms acceptor-type ( $V_{Sc}\text{-}y\text{O}$ ,  $y \leq 4$ ) complexes acting as scattering centers with their formation energy decreasing as the carrier concentration increases.<sup>35</sup> Since isolated  $V_{Sc}$  has relatively high energy of formation,<sup>15</sup> the vacancies produced by implantation can easily associate with the implanted oxygen to form these stable complex-type defects. The complex-like defect contribution to resistivity decreases with respect to the annealing temperature (Table III), which reveals their partial recovery as a function of these temperatures. The slope of the resistivity curves,  $\alpha$ , is also found to decrease toward the reference value with increasing annealing temperature (Table III) suggesting that the electron–phonon scattering interactions are modified by the introduction and recovery of these defects. In the low temperature regime, the resistivity of metals can be usually described by the Bloch–Grüneisen model, taking into account the electron–phonon interactions,

$$\rho(T) = (\rho_R + \rho_{CD}) + A \left( \frac{T}{\theta_D} \right)^n \int_0^{\frac{\theta_D}{T}} \frac{t^n}{(e^t - 1)(1 - e^{-t})} dt, \quad (3)$$

with  $A$  as a constant,  $\theta_D$  the Debye temperature as obtained from the resistivity measurements, and  $n$  a factor that depends on the interaction’s nature.  $\theta_D$  is usually used for quantifying the material stiffness and, thus, retrieves information on the coupling between atoms as  $\theta_D$  is a function of  $\omega_D$ , the maximum frequency for phonon vibrations. It can also be broken down as follows:  $\theta_D = \frac{\hbar\omega_D}{k_B} = \frac{\hbar\bar{v}_s}{k_B} (6\pi^2 n_e)^{1/3}$ , with  $\bar{v}_s$  being the sound velocity and  $n$  the carrier concentration. In the case of ScN films, the resistivity curves were fitted considering the scattering of electrons by phonons; thus,  $n = 5$ .<sup>36</sup> The fit, using Eq. (3), of temperature-dependent resistivity for the reference film [Fig. 5(a)] leads to a Debye temperature close to 900 K, which is higher than the theoretical calculation  $\theta_D \sim 710$  K.<sup>37</sup> Nevertheless, the measured and theoretically calculated temperatures are in good agreement with each other as the theoretical calculations were made for an ideal material, i.e., without defects, and, thus, not considering any unintentional doping and using specific heat, which usually gives lower  $\theta_D$  values. The decrease of  $\theta_D$  toward  $\theta_D$  from the reference film value highlights the recovery of the physical properties of ScN during subsequent annealing. The values of  $\theta_D$  below the one from the reference film can be attributed to an annealing temperature higher than the deposition

temperature, which can modify the residual state or defects that can be present for the as deposited film.

On the other hand, Matthiessen law can be used to describe the mobility [Fig. 4(b)] when the metallic-like behavior is recovered,

$$\frac{1}{\mu(T)} = \frac{1}{\mu_{lat}(T)} + \frac{1}{\mu_R} + \frac{1}{\mu_{CD}}, \quad (4)$$

with  $\mu_{lat} \sim T^{-1.5}$  being the lattice mobility,  $\mu_R$  the residual mobility, and  $\mu_{CD}$  the additional mobility induced by complex-like defects created during the implantation process. The residual mobility was calculated from the reference curve ( $\mu_R = 56 \text{ cm}^2 \text{ V}^{-1} \text{ s}^{-1}$ ) and considered the same for the annealed sample mobilities. The defect contribution  $\mu_{CD}$  on the mobility is listed in Table III. After implantation, the mobility is strongly decreased and is dominated by the as-introduced defects  $\mu_{CD}(\text{O-9 dpa}) = 15 \text{ cm}^2 \text{ V}^{-1} \text{ s}^{-1}$ . According to the Matthiessen law, the contribution from complex-like defects is dominant and overtakes the contribution from the residual state. With increasing annealing temperature,  $\mu$  and  $\mu_{CD}$  are increasing, which shows that the defect contribution on the mobility is decreasing, and thus, that there is recombination of the complex-like defects. Both the resistivity and mobility curves (Fig. 5) exhibit only one slope along the temperature range, which reveals that only one mechanism controls the recombination of these complex defects.

### E. The Seebeck coefficient

For a strongly degenerate semiconductor or an electron gas in a metal, the Seebeck coefficient  $S_d$  is calculated by the following equation:<sup>38</sup>

$$S_d(m^*, n_e, r) = -\frac{k_B}{e} \left( r + \frac{3}{2} \right) \frac{\pi^2}{3} \frac{1}{\eta} \propto m^* n_e^{-\frac{2}{3}} T, \quad (5)$$

where  $r$  is the scattering parameter ( $r = 1.5$  for ionized impurity scattering and  $r = -0.5$  for scattering at acoustical phonons),  $m^*$  the effective mass of the carriers, and  $\eta(n_e, m^*, T) = \frac{[E_F - E_c]}{k_B T}$  the reduced chemical potential ( $E_F$  being the Fermi energy and  $E_c$  the conduction band minimum energy). Based on the fitting of carrier mobilities, showing that the contribution of impurities (residual and implantation-related defects) is not negligible and even prevails after implantation, the Seebeck scattering coefficient was fixed to  $r = 1.5$ . Using Eq. (5) and considering the Fermi gas model, a good

**TABLE III.** Room temperature electrical resistivity and charge carrier concentration, calculated temperature dependence resistivity slope ( $\alpha$ ) [Eq. (2)], additional contribution from the complex-like defects to resistivity ( $\rho_{CD}$ ) and mobility  $\mu_{CD}$ , and the Debye temperature ( $\Theta_D$ ).

	$\rho_{300\text{ K}}$ (m $\Omega$ cm)	$n_e$ ( $\times 10^{20}$ cm $^{-3}$ )	$\alpha$ ( $\times 10^{-4}$ m $\Omega$ cm K $^{-1}$ )	$\rho_{CD}$ (m $\Omega$ cm)	$\mu_{CD}$ (cm $^2$ V $^{-1}$ s $^{-1}$ )	$\Theta_D$ (K) $\pm 5\%$
Reference	0.073	22.1 $\pm$ 2.1	1.2	...	...	912
875 K	0.853	6.7 $\pm$ 0.7	5.2	0.718	16	1169
1075 K	0.486	8.0 $\pm$ 0.8	3.5	0.383	23	986
1175 K	0.343	10.7 $\pm$ 1.1	2.8	0.254	30	931
1275 K	0.244	13.5 $\pm$ 1.4	2.2	0.166	39	897
1375 K	0.188	16.0 $\pm$ 1.6	2.0	0.114	44	878

21 January 2025 14:57:36

fit of  $S_d(T)$  is obtained by taking an effective mass of  $0.68 \pm 0.02 m_0$  for the reference sample ( $m_0$  being the mass of the electron). The reported values for the transport effective mass of electrons in ScN vary between 0.1 and  $0.8 m_0$ ,<sup>16,37,39–41</sup> depending on the calculation or experimental method used. However, this higher effective mass obtained from the fitting of the Seebeck agrees well with Mu *et al.* who showed that the density of states and the transport effective mass were increasing with the electron energy above the conduction band minimum.<sup>40</sup>

The O-9 dpa implanted ScN has temperature-dependent Seebeck behavior that can be expressed as

$$S_d(m^*, n_e, r) \propto m^* n_e^{-\frac{2}{3}} T + S_D, \quad (6)$$

where  $S_D$  is an additional term induced by the implantation-related defects (similar to the additional terms introduced to fit resistivity and mobility,  $S_D = 0$  in the as-grown samples). Using Eq. (6), a value of  $S_D = -17 \mu\text{V K}^{-1}$  is found in the O-9 dpa implanted sample and the effective mass must be reduced to  $m^* = 0.58 \pm 0.02 m_0$ . This model can still be used as the reduction in the number of free carriers leads to a decrease in the Fermi level, which is expected to still be located in the conduction band (ScN remains a degenerate semiconductor according to Mott's criterion). Therefore, the increase of the Seebeck coefficient after implantation in the 100–300 K temperature range is caused by two related factors: the trapping of carriers by the complex-type defects and the decrease of the effective mass due to the decrease of the Fermi level, which is a function of the decrease in the carrier concentration.<sup>40</sup> The relevance or effect behind the additional term remains to be verified, as does the choice of the Seebeck scattering parameter.

Finally, to generate only stable complex defects and enhance the dynamical recombination of point-like defects, an implantation

at 773 K was conducted with the same conditions as the implantation performed at room temperature. The results presented in Fig. 6 align with the predictions from the film annealed *in situ* at 750 K (Fig. 4). Indeed,  $\rho_{773\text{K}}(300\text{ K}) \sim 2.1\text{ m}\Omega\text{ cm}$ , while  $\rho_{750\text{K}}(300\text{ K}) \sim 2.3\text{ m}\Omega\text{ cm}$ . Below 300 K, some light hopping conduction remains (Fig. 6), while above 300 K, the resistivity exhibits metallic-like behavior, showing that the vast majority of point-like defects did not form or were dynamically recombined upon implantation. As the implantation temperature is higher, the annealing dynamic that occurs during collisions is reinforced, which explains why almost no point defects remain after implantation. Similarly, the Seebeck coefficient is also improved compared with the reference film at an intermediate level compared to that implanted at RT. Interestingly, the temperature dependence slope remains rather the same for both implantation but with a lower defect contribution ( $S_D = -7 \mu\text{V K}^{-1}$ ).

## F. Discussion

Substituted oxygen  $O_N$  forms spontaneously in ScN and is the primary source of doping (donors).<sup>12</sup> However, when injected out of equilibrium by the implantation process, no additional *n*-type doping effect is observed: the majority of as-introduced defects are, therefore, of the acceptor-type. This observation remains valid even after thermal annealing at high temperatures, up to 1375 K. Indeed, regardless of the post-treatment after implantation (whether *in situ* or *ex situ* annealing), the concentration of carriers remains lower than the initial doping level (see Secs. III B and III D). In contrast, a strong compensation effect or carrier trapping is observed after implantation ( $\sim 87\%$  of the free carriers are trapped). Our results indicate that this effect arises from at least two mechanisms: the formation of point-like defects and complex-like defects. In the case of point defects, which are responsible for the change in

21 January 2025 14:57:36

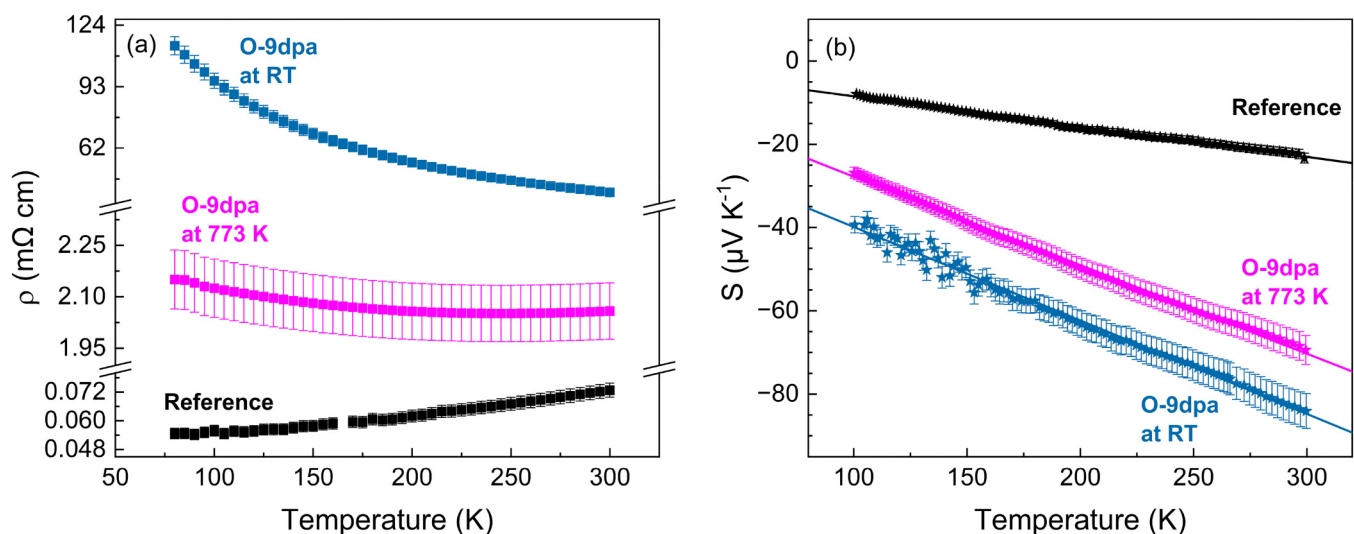


**FIG. 6.** Comparison of the electrical transport properties of the reference and ScN samples (O-9 dpa) implanted at RT and at 773 K: (a) resistivity and (b) Seebeck coefficient, with their respective linear fits in the temperature range of 80–300 K.

the conduction mode, the formation of interstitial oxygen ( $O_i$ ) under implantation is considered. These acceptor-type defects form directly under implantation and are expected to recombine with vacancy defects at “low” temperatures (i.e., between 400 and 750 K), with an activation energy of about 345 meV as discussed in Sec. III C. The maximum concentration of implanted oxygen forming interstitials was estimated from the difference in carrier concentrations of the implanted and the annealed at 750 K state of the film. The variation of charge carrier concentration during *in situ* annealing corresponds to the charge carriers released as the acceptor-type point-like defects recover. Hence, based on the measured carrier concentrations and assuming that  $O_i$  is a single charged acceptor point-like defect (though it can also be doubly charged),<sup>15</sup> there is at most 23 at. % of the implanted oxygen that can be placed on interstitial positions after implantation at RT. Additionally, ballistic point defects are simultaneously created and recombined with  $E_a = 80$  meV, in agreement with what was reported in previous studies.<sup>23,24</sup> The annealing of these point-like defects leads to a decrease of the Mott temperature, which highlights the recombination of these defects.

The implanted oxygen also forms acceptor-type complexes that do not change the conduction mode, as the energy levels they generate are located further from the Fermi level, i.e., within the bandgap. These defects trap the electrons, leading to a decrease of the effective mass, and act also as electron scattering centers, therefore reducing the electron mobility. Their recombination for a higher annealing temperature leads to a recovery of the Debye temperature, which shows the resaturation toward the reference state. These defects are assumed to be of the form ( $V_{Sc}\text{-}yO$ ),<sup>35</sup> which is in good agreement with the study with Ar, where it was shown that argon was trapped by vacancies to form similar complexes.<sup>11</sup> The ( $V_{Sc}\text{-}yO$ ) complexes play here the role of scattering centers for the charge carriers.<sup>35</sup> Experimentally, the mobility is highly decreased even after annealing of the point-like defects [Fig. 5(b)], confirming that the complex-like defects are of the  $V_{Sc}\text{-}yO$  type. Upon post-implantation annealing, these defects agglomerate to form nanocavities. In silicon, nanovoids were reported to act as scattering centers for phonons.<sup>42</sup> As the size of the nanovoids is increased and their number is decreased, the effect on both phonons and electrons was decreased. Therefore, we can expect the same thing to happen with these complex-like defects in ScN.

The power factor  $PF = S^2/\rho$  can be estimated at 600 K from Eqs. (2) and (6) for thermoelectric applications. The reference sample gives a value of  $\sim 2 \times 10^{-3} \text{ W m}^{-1} \text{ K}^{-2}$ , a relatively high value for this level of doping. The O-implanted ScN at 773 K shows a slightly lower value of about  $1.2 \times 10^{-3} \text{ W m}^{-1} \text{ K}^{-2}$ . This decrease should be largely balanced by the reduction in thermal conductivity. The concentration of complex-like defects remaining in the sample is rather large compared to that reported by the noble gas implantation ( $Ar > 3\text{--}4$  dpa) as suggested by the ratio for resistivity  $\Delta\rho_{9\text{ dpa}}^O/\rho_{\text{ref}} \sim 2 \Delta\rho_{>4\text{ dpa}}^{Ar}/\rho_{\text{ref}}$ . Hence, this significant increase in resistivity observed for oxygen implantation is attributed to a higher combined effect of complex-like defects, which results in both a higher trapping effect and carrier mobility scattering [Fig. 5(b)]. Consequently, their high concentration suggests a strong decrease in lattice thermal conductivity. It should be noted that all studies on ScN implantation report a reduction in thermal

conductivity.<sup>10,11,24</sup> Hence, our study of oxygen implantation opens up new possibilities. It is conceivable that by implanting samples with lower dopant concentrations ( $O_N$ ), we can influence carrier concentration through the recovery of point-like defects (such as  $O_i$ ), while simultaneously maintaining complex-type oxygen related defects ( $V_{Sc}\text{-}yO$ ) that impact thermal conductivity. Experiments still need to be conducted to optimize the conditions under which these defects are produced.

#### IV. CONCLUSION

Oxygen implantation was carried out in degenerate ScN thin films to induce doping and introduce defects in order to modify their electrical properties. Studies of the electrical properties demonstrate that the introduction of oxygen ions creates two distinct types of defects, each with unique properties. Point-like defects change the conduction mechanism to hopping by creating localized states close to the Fermi level. Mott temperature analysis shows that oxygen implantation is more effective in creating these point-like defects than noble gases, indicating that both ballistic and chemical effects are at play, particularly involving the nonequilibrium interstitial state of dopants. The thermodynamic recovery of such defects, which begins at 400 K and completes at 750 K, confirms the presence of two types of point defects. More stable complex defects of the ( $V_{Sc}\text{-}yO$ ) type, in line with Density Functional Theory (DFT) calculations,<sup>35</sup> acting as acceptors, increase resistivity and positively enhance the behavior of the Seebeck coefficient. They do not change the conduction mode of ScN and are progressively recombined at higher temperatures. These defects significantly impact electron scattering, reducing their mobility as well as increasing the Seebeck coefficient. These findings open the door to promising fine tuning of the transport properties and, thus, of new technological applications in thermoelectric materials.

#### ACKNOWLEDGMENTS

This work was supported by the French government program “Investissements d’Avenir” (EUR INTREE—Reference No. ANR-18-EURE-0010, LABEX INTERACTIFS—Reference No. ANR-11-LABEX-0017-01, and UP-SQUARED—Reference No. ANR-21-EXES-0013). P.E. and A.L.F. acknowledge funding from the Swedish Government Strategic Research Area in Materials Science on Functional Materials at Linköping University (Faculty Grant SFO-Mat-LiU No. 2009 00971), the Knut and Alice Wallenberg Foundation through the Wallenberg Academy Fellows program (No. KAW-2020.0196), the Swedish Research Council (VR) under Project No. 2021-03826, and the Swedish Energy Agency under Project No. 52740-1.

#### AUTHOR DECLARATIONS

##### Conflict of Interest

The authors have no conflicts to disclose.

##### Author Contributions

**Charlotte Poterie:** Conceptualization (equal); Data curation (equal); Formal analysis (equal); Investigation (equal); Visualization (equal); Writing – original draft (equal). **Hugo Bouteiller:** Conceptualization

(equal); Data curation (equal); Formal analysis (equal); Methodology (equal); Validation (equal); Visualization (equal); Writing – review & editing (equal). **Razvan Burcea:** Conceptualization (equal); Data curation (equal); Formal analysis (equal); Investigation (equal); Methodology (equal); Validation (equal); Visualization (equal); Writing – review & editing (equal). **Sylvain Dubois:** Data curation (equal); Methodology (equal); Resources (equal); Validation (equal); Writing – review & editing (equal). **Per Eklund:** Conceptualization (equal); Funding acquisition (equal); Resources (equal); Writing – review & editing (equal). **Arnaud Le Febvrier:** Conceptualization (equal); Project administration (equal); Supervision (equal); Validation (equal); Writing – review & editing (equal). **Thierry Cabioch:** Conceptualization (equal); Project administration (equal); Supervision (equal); Validation (equal); Writing – review & editing (equal). **Jean-François Barbot:** Conceptualization (equal); Formal analysis (equal); Funding acquisition (equal); Project administration (equal); Resources (equal); Supervision (equal); Writing – review & editing (equal).

## DATA AVAILABILITY

The data that support the findings of this study are available from the corresponding authors upon reasonable request.

## REFERENCES

- <sup>1</sup>B. Biswas and B. Saha, “Development of semiconducting ScN,” *Phys. Rev. Mater.* **3**(2), 020301 (2019).
- <sup>2</sup>S. Kerdsonpanya, N. Van Nong, N. Pryds, A. Žukauskaitė, J. Jensen, J. Birch, J. Lu, L. Hultman, G. Wingqvist, and P. Eklund, “Anomalously high thermoelectric power factor in epitaxial ScN thin films,” *Appl. Phys. Lett.* **99**(23), 232113 (2011).
- <sup>3</sup>P. V. Burmistrova, J. Maassen, T. Favaloro, B. Saha, S. Salamat, Y. Rui Koh, M. S. Lundstrom, A. Shakouri, and T. D. Sands, “Thermoelectric properties of epitaxial ScN films deposited by reactive magnetron sputtering onto MgO(001) substrates,” *J. Appl. Phys.* **113**(15), 153704 (2013).
- <sup>4</sup>J. Kennedy, P. P. Murmu, P. Kumar, and G. Ramanath, “Multifold enhancements in thermoelectric power factor in isovalent sulfur doped bismuth antimony telluride films,” *Mater. Res. Bull.* **142**, 111426 (2021).
- <sup>5</sup>J. R. Sootsman, H. Kong, C. Uher, J. J. D’Angelo, C. Wu, T. P. Hogan, T. Caillat, and M. G. Kanatzidis, “Large enhancements in the thermoelectric power factor of bulk PbTe at high temperature by synergistic nanostructuring,” *Angew. Chem., Int. Ed.* **47**(45), 8618–8622 (2008).
- <sup>6</sup>A. Samarelli, L. Ferre Llin, S. Cecchi, J. Frigerio, D. Chrastina, G. Isella, E. Müller Gubler, T. Etzelstorfer, J. Stangl, Y. Zhang, J. M. R. Weaver, P. S. Dobson, and D. J. Paul, “Prospects for SiGe thermoelectric generators,” *Solid-State Electron.* **98**, 70–74 (2014).
- <sup>7</sup>S. Kerdsonpanya, B. Sun, F. Eriksson, J. Jensen, J. Lu, Y. K. Koh, N. V. Nong, B. Balke, B. Alling, and P. Eklund, “Experimental and theoretical investigation of Cr<sub>1-x</sub>Sc<sub>x</sub>N solid solutions for thermoelectrics,” *J. Appl. Phys.* **120**(21), 215103 (2016).
- <sup>8</sup>N. Tureson, N. Van Nong, D. Fournier, N. Singh, S. Acharya, S. Schmidt, L. Belliard, A. Soni, A. Le Febvrier, and P. Eklund, “Reduction of the thermal conductivity of the thermoelectric material ScN by Nb alloying,” *J. Appl. Phys.* **122**(2), 025116 (2017).
- <sup>9</sup>B. Saha, J. A. Perez-Taborda, J.-H. Bahk, Y. R. Koh, A. Shakouri, M. Martin-Gonzalez, and T. D. Sands, “Temperature-dependent thermal and thermoelectric properties of n-type and p-type Sc<sub>1-x</sub>Mg<sub>x</sub>N,” *Phys. Rev. B* **97**(8), 085301 (2018).
- <sup>10</sup>D. Rao, O. Chowdhury, A. I. K. Pillai, G. K. Pradhan, S. Sahoo, J. P. Feser, M. Garbrecht, and B. Saha, “Multifunctional irradiation-induced defects for enhancing thermoelectric properties of scandium nitride thin films,” *ACS Appl. Energy Mater.* **5**(6), 6847–6854 (2022).
- <sup>11</sup>R. Burcea, J.-F. Barbot, P.-O. Renault, D. Eyidi, T. Girardeau, M. Marteau, F. Giovannelli, A. Zenji, J.-M. Rampoux, S. Dilhaire, P. Eklund, and A. Le Febvrier, “Influence of generated defects by Ar implantation on the thermoelectric properties of ScN,” *ACS Appl. Energy Mater.* **5**(9), 11025–11033 (2022).
- <sup>12</sup>J. S. Cetnar, A. N. Reed, S. C. Badescu, S. Vangala, H. A. Smith, and D. C. Look, “Electronic transport in degenerate (100) scandium nitride thin films on magnesium oxide substrates,” *Appl. Phys. Lett.* **113**(19), 192104 (2018).
- <sup>13</sup>M. A. Moram, Z. H. Barber, and C. J. Humphreys, “The effect of oxygen incorporation in sputtered scandium nitride films,” *Thin Solid Films* **516**(23), 8569–8572 (2008).
- <sup>14</sup>S. Kerdsonpanya, B. Alling, and P. Eklund, “Effect of point defects on the electronic density of states of ScN studied by first-principles calculations and implications for thermoelectric properties,” *Phys. Rev. B* **86**(19), 195140 (2012).
- <sup>15</sup>Y. Kumagai, N. Tsunoda, and F. Oba, “Point defects and p-type doping in ScN from first principles,” *Phys. Rev. Appl.* **9**(3), 034019 (2018).
- <sup>16</sup>R. Deng, B. D. Ozsdolay, P. Y. Zheng, S. V. Khare, and D. Gall, “Optical and transport measurement and first-principles determination of the ScN band gap,” *Phys. Rev. B* **91**(4), 045104 (2015).
- <sup>17</sup>H. Moriceau, F. Mazen, C. Braley, F. Rieutord, A. Tauzin, and C. Deguet, “Smart Cut™: Review on an attractive process for innovative substrate elaboration,” *Nucl. Instrum. Methods Phys. Res. Sect. B* **277**, 84–92 (2012).
- <sup>18</sup>A. Masarrat, A. Bhogra, R. Meena, M. Bala, R. Singh, V. Barwal, C.-L. Dong, C.-L. Chen, T. Som, A. Kumar, A. Niazi, and K. Asokan, “Effect of Fe ion implantation on the thermoelectric properties and electronic structures of CoSb<sub>3</sub> thin films,” *RSC Adv.* **9**(62), 36113–36122 (2019).
- <sup>19</sup>M. M. Timm, E. Oliviero, W. Sun, S. Gomes, G. Hamaoui, P. F. F. Fichtner, and N. Frety, “Ion implantation effects on the microstructure, electrical resistivity and thermal conductivity of amorphous CrSi<sub>2</sub> thin films,” *J. Mater. Sci.* **57**(2), 1174–1185 (2022).
- <sup>20</sup>M. Bala, A. Bhogra, S. A. Khan, T. S. Tripathi, S. K. Tripathi, D. K. Avasthi, and K. Asokan, “Enhancement of thermoelectric power of PbTe thin films by Ag ion implantation,” *J. Appl. Phys.* **121**(21), 215301 (2017).
- <sup>21</sup>A. Bhogra, A. Masarrat, R. Meena, D. Hasina, M. Bala, C.-L. Dong, C.-L. Chen, T. Som, A. Kumar, and A. Kandasami, “Tuning the electrical and thermoelectric properties of N ion implanted SrTiO<sub>3</sub> thin films and their conduction mechanisms,” *Sci. Rep.* **9**(1), 14486 (2019).
- <sup>22</sup>B. Ahmad, R. Meena, P. Kumar, R. Ahmed, M. Hussain, S. M. Tantary, and K. Asokan, “Enhancement of thermoelectrical performance in Au-ion implanted V<sub>2</sub>O<sub>5</sub> thin films,” *RSC Adv.* **7**(80), 50648–50656 (2017).
- <sup>23</sup>R. Burcea, H. Bouteiller, S. Hurand, P. Eklund, J.-F. Barbot, and A. L. Febvrier, “Effect of induced defects on conduction mechanisms of noble-gas-implanted ScN thin films,” *J. Appl. Phys.* **134**(5), 055107 (2023).
- <sup>24</sup>N. Tureson, M. Marteau, T. Cabioch, N. Van Nong, J. Jensen, J. Lu, G. Greczynski, D. Fournier, N. Singh, A. Soni, L. Belliard, P. Eklund, and A. Le Febvrier, “Effect of ion-implantation-induced defects and Mg dopants on the thermoelectric properties of ScN,” *Phys. Rev. B* **98**(20), 205307 (2018).
- <sup>25</sup>A. Le Febvrier, L. Landäl, T. Liersch, D. Sandmark, P. Sandström, and P. Eklund, “An upgraded ultra-high vacuum magnetron-sputtering system for high-versatility and software-controlled deposition,” *Vacuum* **187**, 110137 (2021).
- <sup>26</sup>A. Le Febvrier, J. Jensen, and P. Eklund, “Wet-cleaning of MgO(001): Modification of surface chemistry and effects on thin film growth investigated by x-ray photoelectron spectroscopy and time-of-flight secondary ion mass spectroscopy,” *J. Vac. Sci. Technol. A* **35**(2), 021407 (2017).
- <sup>27</sup>A. Le Febvrier, N. Tureson, N. Stilkirich, G. Greczynski, and P. Eklund, “Effect of impurities on morphology, growth mode, and thermoelectric properties of (1 1 1) and (0 0 1) epitaxial-like ScN films,” *J. Phys. D* **52**(3), 035302 (2019).
- <sup>28</sup>J. More-Chevalier, S. Cichoň, L. Horák, J. Bulíř, P. Hubík, Z. Gedeonová, L. Fekete, M. Poupon, and J. Lančok, “Correlation between crystallization and oxidation process of ScN films exposed to air,” *Appl. Surf. Sci.* **515**, 145968 (2020).

- <sup>29</sup>J. F. Ziegler, M. D. Ziegler, and J. P. Biersack, “SRIM—The stopping and range of ions in matter (2010),” *Nucl. Instrum. Methods Phys. Res. Sect. B* **268**(11), 1818–1823 (2010).
- <sup>30</sup>G. J. Snyder and E. S. Toberer, “Complex thermoelectric materials,” *Nature Mater* **7**(2), 105–114 (2008).
- <sup>31</sup>P. Bougiatioti, O. Manos, C. Klewe, D. Meier, N. Teichert, J.-M. Schmalhorst, T. Kuschel, and G. Reiss, “Electrical transport and optical band gap of NiFe thin films,” *J. Appl. Phys.* **122**(22), 225101 (2017).
- <sup>32</sup>N. F. Mott, “Conduction and switching in non-crystalline materials,” *Contemp. Phys.* **10**(2), 125–138 (1969).
- <sup>33</sup>B. I. Shklovskii and A. L. Efros, *Electronic Properties of Doped Semiconductors* (Springer, Berlin, 1984).
- <sup>34</sup>R. Pilemalm, S. Simak, and P. Eklund, “The effect of point defects on the electronic density of states of ScMN<sub>2</sub>-type (M = V, Nb, Ta) phases,” *Condens. Matter* **4**(3), 70 (2019).
- <sup>35</sup>A. J. E. Rowberg, S. Mu, and C. G. Van De Walle, “First-principles study of hydrogen- and oxygen-related complexes in ScN,” *J. Appl. Phys.* **135**(12), 125701 (2024).
- <sup>36</sup>F. Bloch, “Zum elektrischen Widerstandsgesetz bei tiefen temperaturen,” *Z. Phys.* **59**(3–4), 208–214 (1930).
- <sup>37</sup>B. Saha, J. Acharya, T. D. Sands, and U. V. Waghmare, “Electronic structure, phonons, and thermal properties of ScN, ZrN, and HfN: A first-principles study,” *J. Appl. Phys.* **107**(3), 033715 (2010).
- <sup>38</sup>K. Seeger, *Semiconductor Physics* (Springer, Berlin, 1991).
- <sup>39</sup>A. Qteish, P. Rinke, M. Scheffler, and J. Neugebauer, “Exact-exchange-based quasiparticle energy calculations for the band gap, effective masses, and deformation potentials of ScN,” *Phys. Rev. B* **74**(24), 245208 (2006).
- <sup>40</sup>S. Mu, A. J. E. Rowberg, J. Leveillee, F. Giustino, and C. G. Van De Walle, “First-principles study of electron transport in ScN,” *Phys. Rev. B* **104**(7), 075118 (2021).
- <sup>41</sup>G. Harbeke, E. Meier, and J. P. Dismukes, “Electron effective mass in ScN,” *Opt. Commun.* **4**(5), 335–338 (1972).
- <sup>42</sup>M. T. Dunham, B. Lorenzi, S. C. Andrews, A. Sood, M. Asheghi, D. Narducci, and K. E. Goodson, “Enhanced phonon scattering by nanovoids in high thermoelectric power factor polysilicon thin films,” *Appl. Phys. Lett.* **109**(25), 253104 (2016).